ICAS 2020 SHANGHAI
International Council of the Aeronautical Sciences
32nd Congress of the International Council of the Aeronautical Sciences
September 6-10, 2021
Pudong Shangri-La, Shanghai, China

MODIFICATION OF TURBULENCE MODELS FOR PRESSURE-INDUCED SEPARATION ON SMOOTH SURFACES USING THE DLR VICTORIA EXPERIMENT

Tobias Knopp[1], Matteo Novara[1], Daniel Schanz[1], Wieland Lühder[1], Erich Schülein[1], Reinhard Geisler[1], Florian Philipp[1], Michael Schroll[2], Andreas Krumbein[1], Christian Willert[2] & Andreas Schröder[1]

[1]DLR (German Aerospace Center), Institute of Aerodynamics and Flow Technology, Bunsenstr. 10, 37073 Göttingen, Germany
[2]DLR (German Aerospace Center), Institute of Propulsion Technology, Linder Höhe, 51147 Köln, Germany

Abstract

A new experiment of a turbulent boundary layer flow at a large adverse pressure gradient at a high Reynolds number is presented. The strong pressure gradient leads to pressure-induced separation on the smooth surface of the geometry model with a thin separation bubble. The experiment was performed within the DLR internal project VicToria. First, the design of the test case, the set-up in the wind tunnel, and the measurement technique using both large-scale and high-magnification particle imaging and Lagrangian particle tracking are described. Then the experimental results for the mean velocity are described as the flow evolves downstream from the zero-pressure gradient region into the adverse pressure gradient region. From the measurement data a wall law for the mean velocity with a thin log-law region and a half-power law region above the log-law is observed in the adverse pressure gradient region. Then the differential Reynolds stress transport model SSG/LRR-ω is considered. Based on the observation that the length-scale equation is not consistent with the assumed wall laws at adverse-pressure gradient, a modification of the equation for the dissipation rate ω in the model is proposed, so that the modified model can predict the observed wall law at adverse-pressure gradient. Finally, the numerical results using the modified SSG/LRR-ω model are shown. The modification causes a reduction of the mean velocity in the inner part of the boundary layer at adverse-pressure gradients, making the modified model more susceptible for flow separation. The numerical predictions of the modified model are found to be in good agreement with the experimental data.

Keywords: RANS, turbulent boundary layer, pressure gradient

1. Introduction

The prediction of separation of a turbulent boundary layer on a smooth surface due to an adverse-pressure gradient (APG) in the low-speed regime is of fundamental importance for the accurate prediction of aircraft performance using RANS-based CFD. This issue is still associated with significant uncertainties and open questions. A major problem is that there is no consensus in the research literature on the existence of a wall-law for the mean-velocity profile at adverse pressure gradients which only depends on local flow parameters (see [1], [2]).

The knowledge of a wall law could be used to improve RANS turbulence models similar to the well-known calibration of the length-scale equation for the log-law at zero-pressure gradient (see [3]). There has been a noticeable increase in the research activity on turbulent boundary layer flows in adverse pressure gradient since the seminal 1968 conference [4]. During the past years, both new experimental studies, e.g., [5], [6], [7] and studies using direct numerical simulations (DNS) have been performed, e.g., [8], [9], [10]. Regarding their relevance for the flow around aircraft wings near maximum lift in the low-speed regime, characteristic features are the very high Reynolds numbers and the onset of incipient flow separation in conjunction with thin regions of separated flow near

the surface. The number of well-defined and documented validation test cases are still rare in the literature. The flow features involved in flows with pressure gradient and separation are often even more complex, if surface curvature plays a significant role [11].

For these reasons, a new boundary-layer experiment was designed and performed within the DLR project VicToria. The experiment is based on two earlier experiments conceived by DLR and performed in cooperation with the Universität der Bundeswehr München (UniBw). Regarding these two precursor experiments, the first joint DLR/UniBw experiment was performed within the DLR project RETTINA in 2011. This experiment was at moderately large Reynolds numbers up to $Re_\theta = 10000$ of the incoming boundary layer before entering the APG region, see [12] and [13]. The second experiment was performed within a common DFG project "Investigation of turbulent boundary layers with pressure gradient at high Reynolds numbers with high-resolution multi-camera techniques" by DLR AS and UniBw Munich (Grant KA 1808/14-1 and SCHR 1165/3-1). It was performed at higher Reynolds numbers up to $Re_\theta = 30000$ of the incoming boundary layer upstream of the APG region, and the adverse-pressure gradient was moderately strong but the flow remained attached and was remote from separation, see [14] and [15]. The third experiment is subject of the present paper. The geometry model is based on the second experiment, but the downstream end of the geometry was modified to increase the adverse-pressure gradient and to cause a thin separation bubble.

The goals of the experiment are (i) to establish a data base for the mean velocity and the Reynolds stresses in the APG region and in the separation region, and (ii) to extend a recently proposed wall-law at APG (see [16]) towards separation. A principal aim (iii) is to provide a new well-defined and documented test case as a validation case for both RANS and hybrid RANS/LES methods. Finally, aim (iv) is to revisit the recently proposed modification of the ω-equation for SSG/LRR-ω differential Reynolds-stress model (DRSM), see [17], and to calibrate this modification as the flow is approaching separation.

The main underlying question is the existence of a wall-law for the mean velocity in the inner layer, which depends on local flow parameters. The present work is based on the following ideas. The first idea is that there still exists a logarithmic region under APG conditions, which becomes smaller as the flow approaches separation, see [18], [2], and [15], and that there is a systematic reduction of the extent of the log-law region at APG, see [16], which was found for Couette-Poisseuille flow by [19]. Additionally, the proposal by Nickels in [20] is used, stating that the log-law slope coefficient is assumed to decrease with increasing values of the pressure-gradient parameter in inner viscous scaling. The next idea follows [21], who proposed that, above the log-law, a half-power law (or square-root law) emerges, extending to the wall distance the log-law typically occupies at zero pressure gradient. Experimental support for these hypotheses was already found from the results of the first and second joint DLR/UniBw experiment, cf. [12] and [15]. In the present work we use the square-root law (sqrt-law) formulation introduced in [22]. The aim of this experiment is to study the above hypotheses for a high-Re flow with incipient separation.

The status of work on the improvement of RANS models for turbulent boundary layers at adverse-pressure gradient is rare in the literature. One of the few attempts to modify k-ω-type turbulence models for APG was the proposal by Rao and Hassan [23]. Their idea was to modify the equation for the turbulent kinetic energy k, so that the modified model gives the sqrt-law for the mean velocity at APG. Rao and Hassan propose to modify the model for the turbulent diffusion of k by taking into account an additional modeling term which may be associated with the diffusion due to pressure fluctuations and which scales with the streamwise component of the mean pressure gradient. This idea was studied and modified in [16] for the SST k-ω model [24]. As a second idea presented in [16], the model coefficient of the ω-equation which controls the slope of the log-law was made a function of the pressure-gradient parameter following the idea by [20]. The underlying idea of both modifications is to make the turbulence model more sensitive to flow separation by reducing the turbulent shear stress in the near wall region by increasing the dissipation of turbulence ε. The present work focusses on the SSG/LLR-ω model [25], [26]. In [17], the pressure diffusion term was used to modify only the ω-equation. Noteworthily, the improvement of RANS models in the inner part of the turbulent boundary layer are expected to improve the predictive accuracy of hybrid RANS/LES methods [27] for pressure induced separation on a smooth surface.

The impressive improvements in measurement techniques in past decade are an additional motivation for new wind-tunnel experiments for turbulent boundary layers at adverse-pressure gradient. In the present work we combine particle image velocimetry (PIV) in a large-scale overview measurement set-up and Lagrangian particle tracking velocimetry at selected locations for the volumetric measurement of all three-components of the mean velocity, see [28, 17, 29, 30].
The paper is organized as follows: In the first part, sections 2 and 3, we describe the DLR VicToria experiment, the measurement techniques and the experimental results. Then, in sections 4 and 5, we describe a modification for the ω-equation for adverse-pressure gradients for the SSG/LRR-ω model, which was recently proposed in a first version for the SST model in [24]. In section 6 we apply the modified SSG/LRR-ω model to the VicToria experiment. Our conclusions are drawn in section 7.

2. Wind-tunnel experiment

2.1 Experimental set-up

The experiment was performed in the Eiffel type atmospheric wind tunnel (AWM) of UniBw in Munich. It features a 22-m-long test section and a cross section of $1.8 \times 1.8\,\mathrm{m}^2$. In the context of the present investigation the origin $x = 0$ is defined at a position located $0.87\,\mathrm{m}$ downstream of the smallest diameter of the wind tunnel's contraction. As described in figure 1 (left), the flow develops along the plain wind tunnel wall over a streamwise distance of $4.575\,\mathrm{m}$. Then the flow is accelerated along a first ramp of height $0.444\,\mathrm{m}$ and of length $1.732\,\mathrm{m}$. Then the flow relaxes over a flat plate of length $4.0\,\mathrm{m}$ at (almost) ZPG. A reference position for the incoming boundary layer is at $x = 8.629\,\mathrm{m}$. In the focus region, the flow follows a first curvilinear deflection of length $0.760\,\mathrm{m}$, which initially causes a small favourable pressure gradient (FPG), and then enters into the APG region with a second curvilinear deflection of length $0.320\,\mathrm{m}$. The APG focus region is on the inclined flat plate of length $0.762\,\mathrm{m}$ at an opening angle of around $18.6°$. Note, that this flat plate has an insert for a glass plate, providing good optical access for PIV measurements. The small divergence angle of the wind tunnel walls is around $0.13°$. The two other wind tunnel walls are parallel.
The model's geometry was designed using two-dimensional RANS simulations with the DLR TAU code using the SA- and SST-model, and for some configurations using the SSG/LRR-ω mode. The aim of the RANS design study was to obtain flow separation in the last part of the glass plate. The advantage of PIV measurements through the glass plate is to avoid reflections at the aluminium surface of the test model which allows for data to be acquired very close to the wall. The experiments were performed at different values for the free-stream velocity to obtain a variation of the Reynolds number and of the separation line. The measurements of the first of two measurement campaigns were performed four different values for the free-stream velocity. The boundary layer edge velocity measured at the reference position at $x = 8.629\,\mathrm{m}$ was $U_{\mathrm{ref}} = 21.1\,\mathrm{m/s}$, $26.6\,\mathrm{m/s}$, $29.3\,\mathrm{m/s}$, and $35.5\,\mathrm{m/s}$.

2.2 Flow conditions

The focus here is on the case at the highest Re at $U_{\mathrm{ref}} = 35.5\,\mathrm{m/s}$ measured at $x = 8.629\,\mathrm{m}$. The velocity at the entrance into the test section was $21.41\,\mathrm{m/s}$. The characteristic boundary layer parameters are summarized in table 1. The reported streamwise positions are the reference position at $x = 8.629\,\mathrm{m}$ and at the position $x = 10.548\,\mathrm{m}$ in the adverse pressure gradient region, being the position of the 3D3C multi-pulse STB measurements. The table summarises Reynolds number Re_θ based on the momentum thickness θ and $Re_\tau = u_\tau \delta_{99}/\nu$ based on the friction velocity u_τ and the 99% boundary layer thickness δ_{99}. Moreover the pressure gradient parameter in inner viscous scaling $\Delta p_s^+ = \nu/(\rho u_\tau^3)\mathrm{d}P/\mathrm{d}s$ and in Rotta-Clauser scaling β_{RC}, and the shape factor H_{12} are also summarised in table 1.
The streamwise distribution for the pressure coefficient c_p and for $\mathrm{d}c_p/\mathrm{d}s$ along the centerline are shown in figure 1 (right). The pressure gradient along the contour in different scalings is shown in figure 2. The pressure gradient parameter Δp_s^+ in the inner scaling for the inner part of the boundary layer ($y < 0.2\delta_{99}$) is shown in figure 2 (left). Note that $10\Delta p_s^+$ is shown in this figure, i.e., Δp_s^+ is scaled by a factor of ten. As the flow approaches separation, $u_\tau \to 0$ and this increases the values for Δp_s^+. Large values of $\Delta p_s^+ > 0.05$ are present over a significant streamwise distance in the region of the strong APG. The pressure gradient in the scaling for the outer part using the proposal by Zagarola &

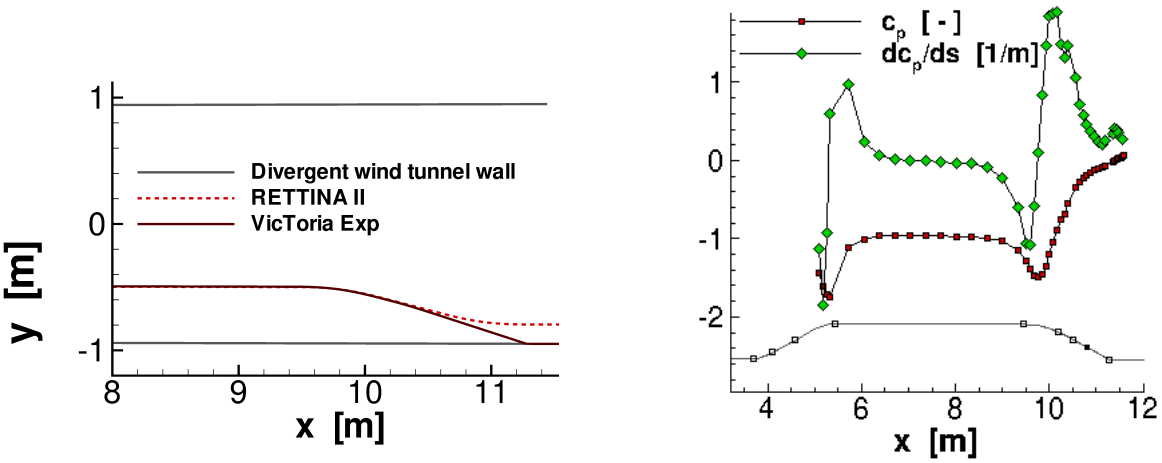

Figure 1 – Sketch of the model geometry of the DLR VicToria experiment mounted to the wind-tunnel wall (left) and streamwise c_p and $\mathrm{d}c_p/\mathrm{d}s$ along the contour as measured along the centerline (right).

Table 1 – Characteristic boundary layer parameters for the case $U_{\mathrm{ref}} = 35.5\,\mathrm{m/s}$ for the 2D2C PIV measurements at two streamwise positions.

	x in m	U_e in m/s	Re_θ	Re_τ	δ_{99} in mm	H_{12} in mm	u_τ in m/s	Δp_s^+	β_{RC}
ZPG	8.629	35.5	22634	9308	117.7	1.23	1.24	-0.0004	-0.39
APG	10.548	30.7	47576	4620	195.5	1.81	0.40	0.16	151.1

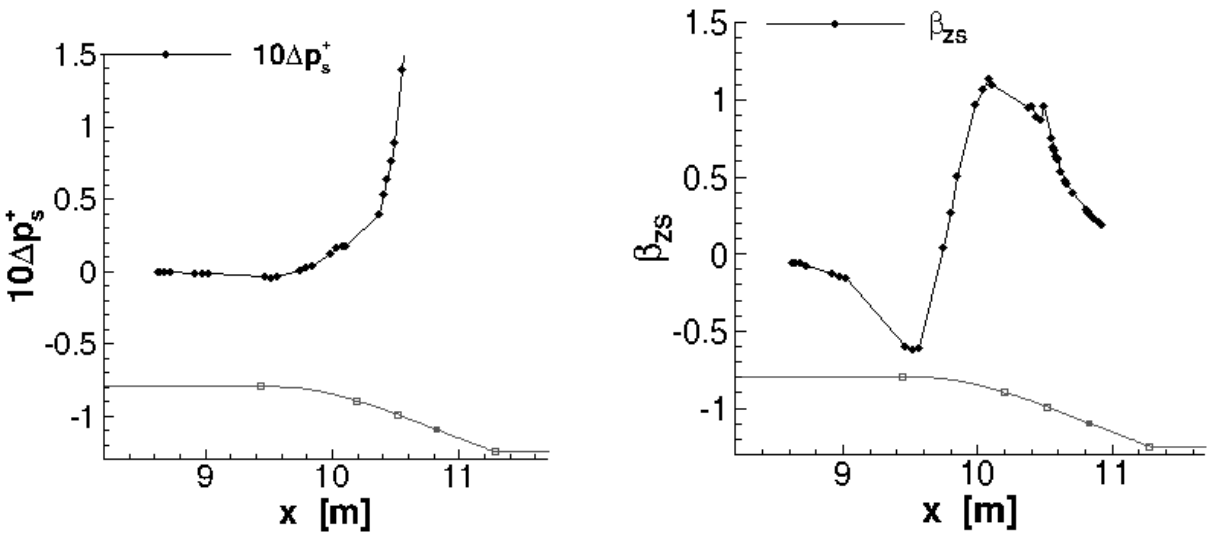

Figure 2 – Streamwise distribution of the pressure gradient parameter in the inner scaling Δp_s^+ (left) and in the scaling by Zagarola & Smits β_{ZS} (right).

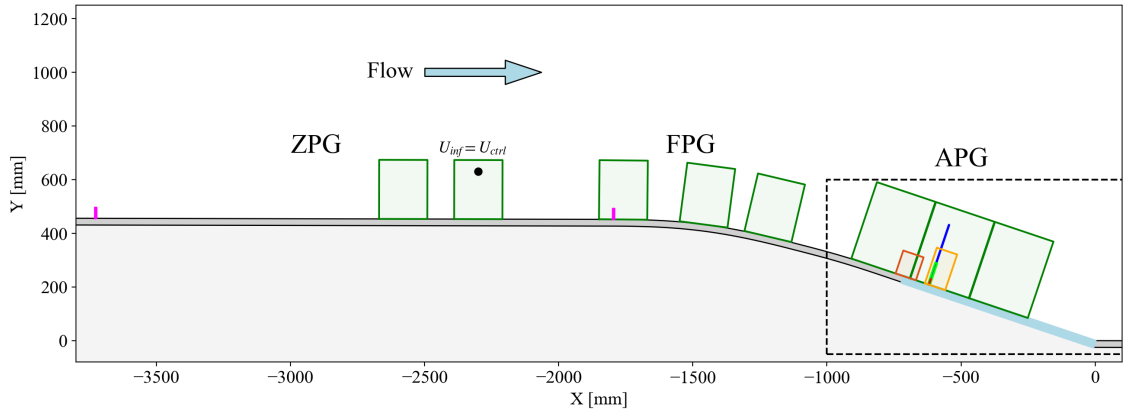

Figure 3 – Overview of the measurement locations for various employed particle imaging techniques.

Smits β_{ZS} is shown in figure 2 (right). For the fluid parameters in the wind-tunnel for the 2D2C PIV measurements, the values are kinematic viscosity $\nu = 1.700\,\mathrm{m^2 s^{-1}}$, density $\rho = 1.088\,\mathrm{kgm^{-3}}$, reference pressure $p = 94182\,\mathrm{Nm^{-2}}$ and temperature $T = 299.68\,\mathrm{K}$.

2.3 Measurement technique

2.3.1 Flow field measurement

For the flow field measurements a combination of different particle imaging approaches was used. Figure 3 gives an overview of the measurement locations for various employed particle imaging techniques and of the fields of view for the large-scale overview measurement. A multi-camera large-scale 2D2C-PIV system comprising 8 cameras was applied to simultaneously measure the evolution of the mean velocity from the zero-pressure gradient region to the adverse pressure gradient region and the region of separation. As indicated in figure 3 each field of view was $0.2 \times 0.25\mathrm{m}^2$ in streamwise and wall-normal direction and contained the boundary layer edge. The field was enlarged to $0.2 \times 0.3\mathrm{m}^2$ in the adverse pressure gradient region to capture the outer edge of the boundary layer. For the evaluation of the 2D2C-PIV data, conventional coarse-to-fine cross-correlation analysis was used. The final interrogation window size was set to $24 \times 14\mathrm{px}^2$ corresponding to approximately $2 \times 1.2\mathrm{mm}^2$ and $2.7 \times 1.6\mathrm{mm}^2$ in the ZPG and APG regions respectively.
High-resolution measurements were performed at selected locations in the ZPG, FPG and ZPG re-

gions using both a high-speed 2D2C-profile PIV measurement technique [31] as well as 3D3C Lagrangian particle tracking velocimetry (PTV) using the in-house developed Shake-The-Box (STB) method [28]. The 2D2C-profile PIV measurements were performed at camera frame rates up to 50 kHz at spatial resolutions nearly matching the viscous length scales ($\nu/u_\tau \approx 13-25\mu$m), thereby providing access to the temporally evolving wall shear stress. For analysis a 2D2C-STB approach derived from the 3D3C-STB algorithm was used. The STB measurements made use of both a multi-pulse acquisition strategy (MP-STB) [29, 30] as well as a time-resolved mode (TR-STB) [28]. For multi-pulse STB, the field of view was $80\times90\times7\,\mathrm{mm}^3$ while the 3D3C-TR-STB imaged a volume of $9\times85\times2\,\mathrm{mm}^3$ at imaging frequencies up to 40 kHz.
Both the 3D3C-TR-STB and the high-speed 2D2C-profile PIV measurement technique additionally provide access to data that are highly-resolved in both space and time, but are not considered in the present context. Further details on the employed measurement techniques are provided in [32].

2.3.2 Skin friction measurement

For accurate skin-friction measurements the non-intrusive Oil-Film Interferometry (OFI) technique is used. To perform wall shear stress measurements using OFI in the general case of a three-dimensional flow, precise knowledge of the limiting-streamline topology and the oil properties (viscosity, density, refractive index) over the entire wall temperature range are essential in addition to the distribution of the temporal oil film thinning rate.
The approach applied at the AWM uses the white-light oil-film interferometry to automatically determine both the local wall streamline directions and the temporal oil-film-thickness variations from individual interference images. The necessary background illumination was realized by means of special diffuse LED light fields (0.6m $\times$ 0.6 m), which were developed and fabricated in advance for measurements on large-scale models. The use of three separate color LED types (in red, green and blue) enables highly accurate reconstruction of the oil film thickness according to the principle of white light interferometry. In order to achieve an optimum contrast of the interference images the model surface was coated on site with a self-adhesive black PVC high-gloss film (thickness approx. 0.1mm). Two industrial CMOS cameras from SVS-VISTEK, which are robust enough and do not require additional cooling in wind tunnel operation, were used to enable simultaneous OFI measurements in two overlapping areas of the model surface. A very low viscosity silicone oil ELBESIL B5 (5 cSt at 25°C) was used in the tests. The temperature dependence of the oil viscosity was checked by means of a viscometer over the entire relevant temperature range in order to keep the measurement inaccuracies as small as possible. Before each new OFI test, the test surface was cleaned and a new oil strip was applied perpendicular to the longitudinal axis of the model in the test area. The flow-induced change in the surface distribution of the oil film thickness was optically recorded during the test period and documented in each case as a sequence of oil film interference images. The interference images obtained were first rectified and then evaluated to determine the wall flow line topology as well as the temporal change in the local oil film thickness in order to subsequently calculate a surface distribution of the wall shear stress.

3. Experimental results

In this section, the results for the mean velocity profiles in the adverse pressure gradient region are presented. The data are normalized using viscous units

$$u^+ = \frac{U}{u_\tau}, \quad y^+ = \frac{y u_\tau}{\nu}, \quad \alpha^+ \equiv \Delta p_s^+ = \frac{\nu}{\rho u_\tau^3}\frac{\mathrm{d}P}{\mathrm{d}s} \tag{1}$$

Here the friction velocity u_τ is determined using a Clauser chart applied to the mean velocity profiles obtained with 2D2C PIV. Moreover, oil film interferometry measurements were performed as a complementary technique. For the MP-STB data, u_τ was determined by a least-squares fit of the MP-STB data to the mean velocity profile inferred from the DNS data [33] for $y^+ < 20$, which are at a similar value of Δp_s^+.
The log-law is found to be a robust feature in the mean velocity profiles. Even for large values of Δp_s^+, a thin region can be found, where the mean velocity profile can be fitted by the log-law, see figure 5

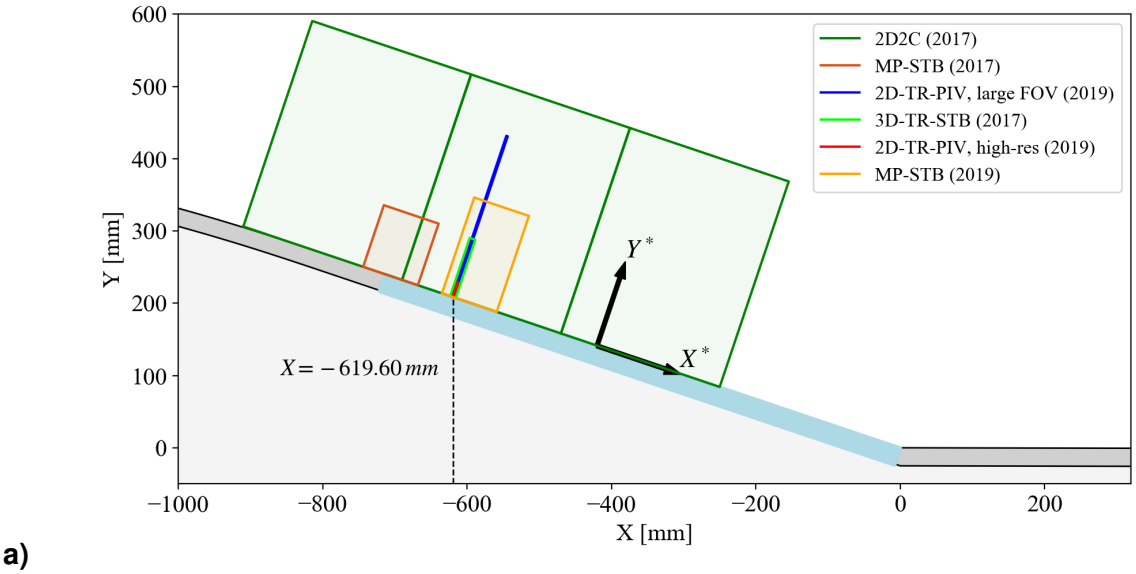

a)

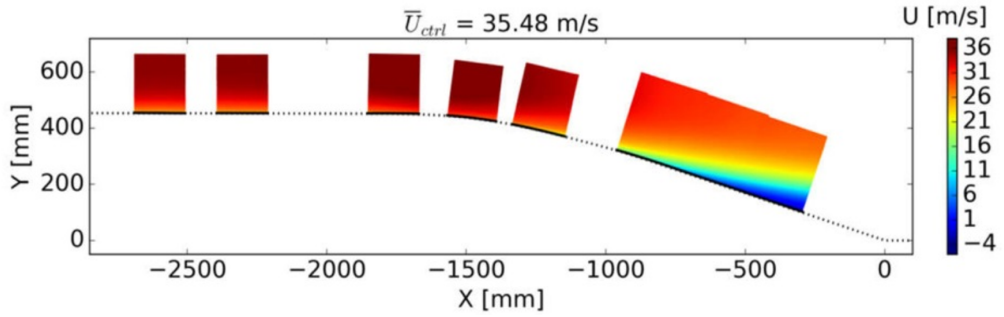

b)

Figure 4 – (a) Detail of measurement domains near the point of flow separation; (b) mean streamwise velocity distribution at $U_{\mathrm{ref}} = 35.5\,\mathrm{m/s}$ obtained with large-scale 2D2C-PIV.

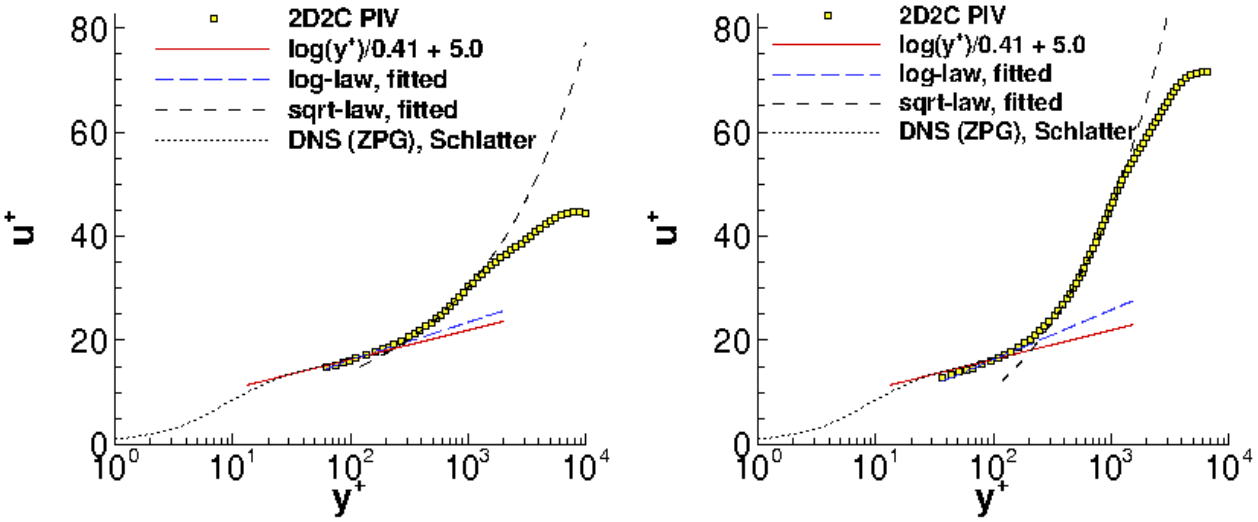

Figure 5 – Left: Mean velocity profiles in the adverse pressure gradient region at the station $x = 10.38\,\mathrm{m}$ at $\Delta p_s^+ = 0.018$ (left) and at the station $x = 10.55\,\mathrm{m}$ at $\Delta p_s^+ = 0.060$ (right).

(right),

$$u^+ = \frac{1}{\kappa}\log(y^+) + B \tag{2}$$

This is seen as a further indication in support for the resilience of the logarithmic law for the mean velocity to pressure gradients reported by [2].
For a more detailed study of the log-law region, the extent of the log-law fit region was determined in terms of y^+ for each velocity profile. The interval, where the mean velocity profile can be fitted by a log-law, was chosen by visual inspection. For a moderately strong APG, the log-law was found in the region $70 < y^+ < 140$ For a strong APG, the log-law was observed in the region $20 < y^+ < 80$. The upper edge of the log-law region was found to be further decreasing while approaching separation.
Above the log-law region, a half-power law (or square-root law, abbreviated sqrt-law) emerges, see figure 5 (right). The sqrt-law is written here in the form

$$u^+ = \frac{1}{K}\log(y^+) + \frac{2}{K}\left(\sqrt{1+\Delta p_s^+ y^+} - 1\right) + \frac{2}{K}\log\left(\frac{2}{\sqrt{1+\Delta p_s^+ y^+}+1}\right) + B_o \tag{3}$$

This observation is seen to support the proposal by [21] that, above the log-law, a half-power law (or square-root law) emerges.
The MP-STB data for the mean velocity profile and the composite wall-law are shown in figure 5 (right).
Regarding the variation of the von Kármán constant κ, a value of $\kappa = 0.293$ was found from the MP-STB data at $x = 10.548\,\mathrm{m}$ in the region of the strong APG. We found in [14] that the reduction can be described for moderate APG by the following model provided by Nickels [20]

$$\frac{\kappa}{\kappa_0} = \sqrt{\frac{1}{1+\Delta p_s^+ y_c^+}} \tag{4}$$

Here κ_0 is the value for turbulent boundary layers at ZPG and y_c^+ is associated with the thickness of the viscous sublayer, which is a decreasing function of Δp_s^+ in the work of [20].

4. RANS turbulence modelling

For RANS turbulence modelling, we consider the differential Reynolds stress model SSG/LRR-ω. This model is the starting point for the RANS model modification. The model has been validated for a broad range of aerodynamic flows and has demonstrated its maturity for complex industrial aircraft

configurations in a large number of applications. The transport equation for the Reynolds stresses $\overline{u_i' u_j'}$ can be written in the form

$$\frac{\partial \overline{u_i' u_j'}}{\partial t} + \frac{\partial}{\partial x_k}\left(U_k \overline{u_i' u_j'}\right) = P_{ij} + \Pi_{ij} - \varepsilon_{ij} + D_{ij}^{\nu} + D_{ij}^{t} + D_{ij}^{p} \tag{5}$$

Here P_{ij} denotes production, ε_{ij} denotes dissipation, D_{ij}^{ν} and D_{ij}^{t} denote the viscous and turbulent transport of $\overline{u_i' u_j'}$, and D_{ij}^{p} denotes the transport due to pressure fluctuations (or pressure diffusion), see [26]. The corresponding equation for the turbulent kinetic energy $k = \frac{1}{2}\overline{u_i' u_i'}$ follows from (5)

$$\frac{\partial k}{\partial t} + \vec{\nabla}\cdot(\vec{U}k) = P_k - \varepsilon + D_k^{\nu} + D_k^{t} + D_k^{p} \tag{6}$$

In the SSG/LRR-ω model, ε is computed from the specific dissipation rate ω, that is, $\varepsilon = \beta_k k\omega$. In the inner part of the boundary layer, the transport equation for ω is given by

$$\frac{\partial \omega}{\partial t} + \vec{\nabla}\cdot(\vec{U}\omega) - \vec{\nabla}\cdot\left((\nu + \sigma_\omega \nu_t)\vec{\nabla}\omega\right) = \frac{\gamma}{\nu_t} P_k - \beta_\omega \omega^2 \tag{7}$$

which can be written in the form

$$\frac{\partial \omega}{\partial t} + \vec{\nabla}\cdot(\vec{U}\omega) - D_\omega^{\nu} - D_\omega^{t} = P_\omega - \varepsilon_\omega \tag{8}$$

with viscous and turbulent diffusion terms D_ω^{ν}, D_ω^{t}, production term P_ω and dissipation term ε_ω.

4.1 Modification to account for the half-power law

The boundary layer analysis of the ω-equation at APG, using the assumptions that the mean velocity profile follows a sqrt-law and that the total shear stress is growing as a linear function of the wall-distance, was described in [16] and [17]. It was shown that the ω-equation is not consistent with the assumed solution in the sqrt-law region at APG. From this analysis a model discrepancy term m_ω^+ for the sqrt-layer was inferred. The discrepancy term can be expressed using the pressure diffusion term D_k^p proposed for the k-equation by [23]. The pressure diffusion term for the ω-equation becomes

$$-D_\omega^p = -\frac{\omega}{k}\frac{\partial}{\partial x_j}\left(\sigma_{k,P}\nu_t \frac{\partial P}{\partial x_i}\frac{b_{ij}}{\rho}\right) \quad \text{if} \quad \Delta p_s^+ > 0 \tag{9}$$

and is set to zero for $\Delta p_s^+ \leq 0$. The anisotropy tensor b_{ij} is given by

$$b_{ij} = \frac{\tau_{ij}}{\rho k} + \frac{2}{3}\delta_{ij}\ , \quad \tau_{ij} = -\rho\overline{u_i' u_j'}. \tag{10}$$

The coefficients of the pressure diffusion term are given by

$$\sigma_{\omega,P} = \sigma_\omega \lambda \beta_k^{-1}, \quad \beta_k = 0.09\,, \quad \lambda = 0.7 \tag{11}$$

The pressure diffusion term is only activated in the assumed sqrt-law region. For this purpose, the blending functions f_{b2} and f_{b3} are used, which are described in detail in [16]. The modified ω-equation with the additional pressure diffusion term D_ω^p and with the blending functions f_{b2}, f_{b3} becomes

$$\frac{\partial \omega}{\partial t} + \vec{\nabla}\cdot(\vec{U}\omega) - D_\omega^{\nu} - D_\omega^{t} - f_{b2}f_{b3}D_\omega^{p} = P_\omega - \varepsilon_\omega \tag{12}$$

The blending function f_{b2} describes the progressive breakdown of the log-law in APG. It accounts for the modelling hypothesis that the outer edge of the log-law region is decreasing with increasing Δp_s^+. The function f_{b2} has a value of zero in the near wall region and in the log-law region, increases in the transition region, and has a value of one in the sqrt-law region. On the other hand, the function f_{b3} has a value of one in the inner part of the boundary layer and approaches zero for $y > 0.15\delta_{99}$.

4.2 Modification for a change of the log-law slope

The second idea is to sensitize the value of κ with respect to Δp_s^+ using the following relation among the coefficients of the k-ω model for the log-law, see [34],

$$\gamma = \gamma(\kappa(\Delta p_s^+)) = \frac{\beta_\omega}{\beta_k} - \frac{(\kappa(\Delta p_s^+))^2 \sigma_\omega}{\sqrt{\beta_k}} \tag{13}$$

Here $\kappa(\Delta p_s^+)$ is given by (4). For each field point, Δp_s^+ is given by the value at the nearest wall point. At APG, $\kappa(\Delta p_s^+)$ decreases when Δp_s^+ is increasing, and hence γ is increasing. Then the production term of ω is increasing, which causes an increase in $\varepsilon = \beta_k k\omega$. This, in turn, causes a reduction of the turbulent shear stress, which makes the model more susceptible for flow separation. Note that the modification of γ needs to be deactivated in the near-wall region using an additional blending function, see [16].

5. Numerical method

For the numerical RANS simulations, the TAU-code developed by DLR is used, which features an unstructured solver for the compressible Navier-Stokes equations, see e.g. [35]. The inviscid fluxes are calculated by a 2nd-order central method with artificial matrix-valued or scalar-valued dissipation [36]. For the discretization of the equation for k and ω, a second order Roe scheme is used in this work.

The simulations are performed using an extended data structure within TAU, see [16]. This data-structure provides, for every wall node, a list of field points lying on an approximately wall-normal line. Then the surface data like u_τ and Δp_s^+ can be extrapolated into the field along wall-normal lines. Moreover for each surface point the boundary layer thickness δ_{99} can be determined. For more details, see [37, 38, 39].

6. Numerical results

6.1 Numerical set-up

For the RANS simulations of the DLR VicToria Experiment, the computational set-up considers two-dimensional simulations of the flow in the mid-span of the wind tunnel. The wind-tunnel walls have a small divergence angle, which are given by the experimental set-up and used in the numerical set-up. The hybrid meshes were generated using the mesh generation tool CentaurSoft. Regarding the mesh resolution, the mesh spacing in streamwise direction is $0.014\mathrm{m}$ in the focus region of curvature and pressure gradient. The boundary layer is resolved using more than 100 grid nodes. The first node above the wall is at around $y^+ = 1.4$ in the zero pressure gradient region at $x = 8.6\mathrm{m}$, and $y^+ < 1$ in the APG region. The total number of mesh points of the corresponding two-dimensional grid is 220000.

Regarding the RANS modelling, the simulations used the SA model, the SST model and the SSG/LRR-ω model. Moreover the modified version of the ω-equation within the SSG/LRR-ω model using the equation (12) with the pressure diffusion term is applied. In the figures this version is denoted by "mod sqrt". The version which uses additionally the modification (13) for κ is not shown here.

For the computational set-up, the geometry of the wind tunnel was modified in order obtain a matching between the RANS models and the experimental data at the reference position at $x = 8.629\mathrm{m}$. If using the exact geometry of the test-section of the wind-tunnel, the boundary layer thickness δ_{99} and the integral boundary layer thickness quantities for the displacement thickness δ^* and for the momentum-loss thickness θ at $x = 8.629\mathrm{m}$ obtained from the different RANS models were found to be systematically smaller than for the experimental data, independent of the RANS model. For this purpose, in the computational set-up, the length of the test-section upstream of the contour model was increased in order to match δ^* at $x = 8.629\mathrm{m}$.

6.2 Zero-pressure gradient region

The results in the zero-pressure gradient region are studied first. The focus is on the adjusted computational set-up using a larger length for the development of the upstream boundary layer on the wind tunnel wall. We first consider the reference position at $x = 8.629\mathrm{m}$. Concerning the mean velocity profile, the results for the RANS models SA, SST and SSG/LRR-ω are close to each other

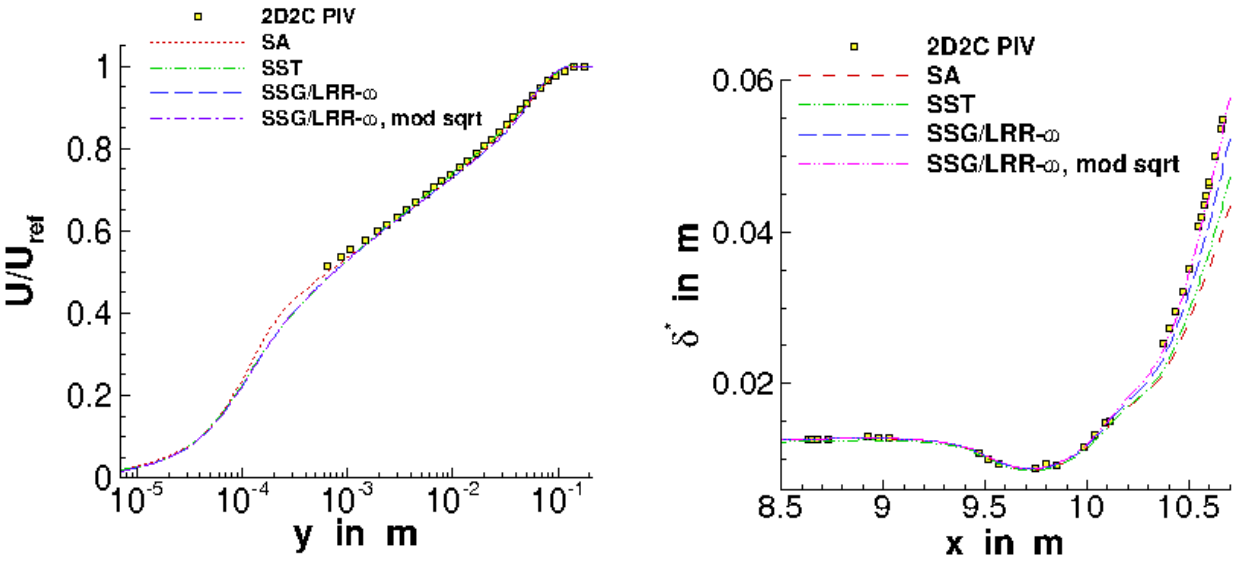

Figure 6 – Left: Mean velocity profiles at the reference position at $x = 8.629\mathrm{m}$ at almost zero pressure gradient. Right: Streamwise distribution of the displacement thickness δ^*.

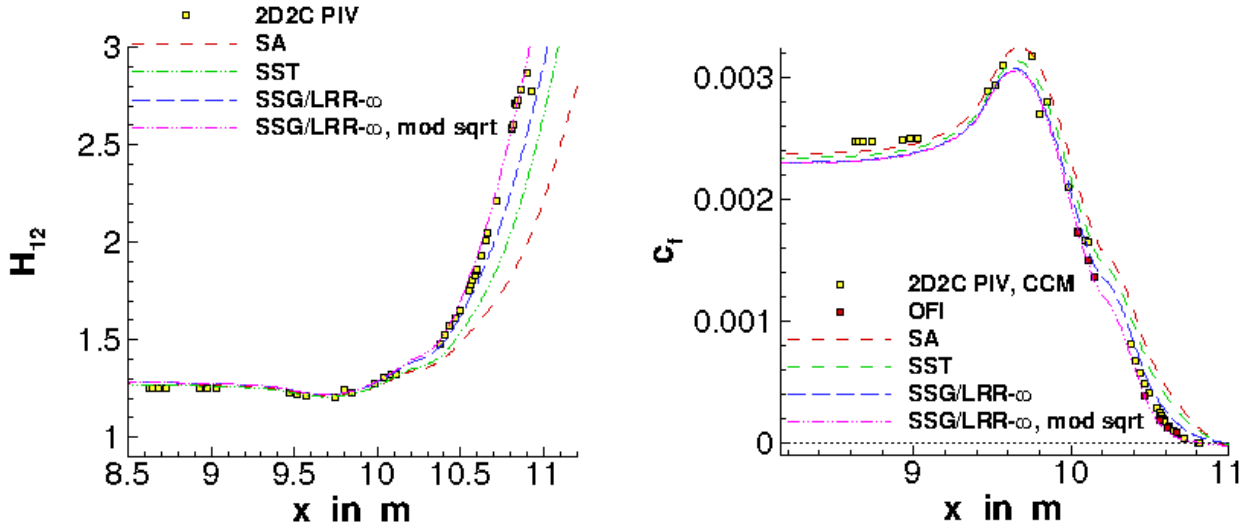

Figure 7 – Streamwise distribution for the shape factor H_{12} (left) and for the skin friction coefficient c_f (right). A Clauser chart method (CCM) was used to determine c_f for the 2D2C PIV.

and closely match the experimental PIV data, see figure 6 (left). The displacement thickness δ^* for the different RANS models is also found to be in a good agreement with the experimental results, as shown in figure 6 (right). The shape factor $H_{12} = \delta^*/\theta$ also shows a good agreement between RANS and experiment, see figure 7 (left). The values for the skin-friction coefficient c_f are found to be underestimated by the RANS simulations in comparison to the experimental data, see 7 (right). The values for the wall-shear stress were determined using the standard Clauser chart method from the 2D2C PIV data. This deviation in c_f is seen as a compromise. Since the flow at $x = 8.629\mathrm{m}$ is not a perfectly canonical turbulent boundary layer, it is not possible to match both c_f and δ^* using a straight wind tunnel wall for the development of the upstream boundary layer.

6.3 Adverse pressure gradient region

Downstream of the reference position at almost zero pressure gradient, the flow enters the region of curvature in conjunction with a favourable pressure gradient. Then, still in the region of curvature, the streamwise pressure gradient switches from favourable to adverse. For the position $x = 9.85\,\mathrm{m}$ the mean velocity profiles are shown in figure 8 (left). The results for the SST model and for the

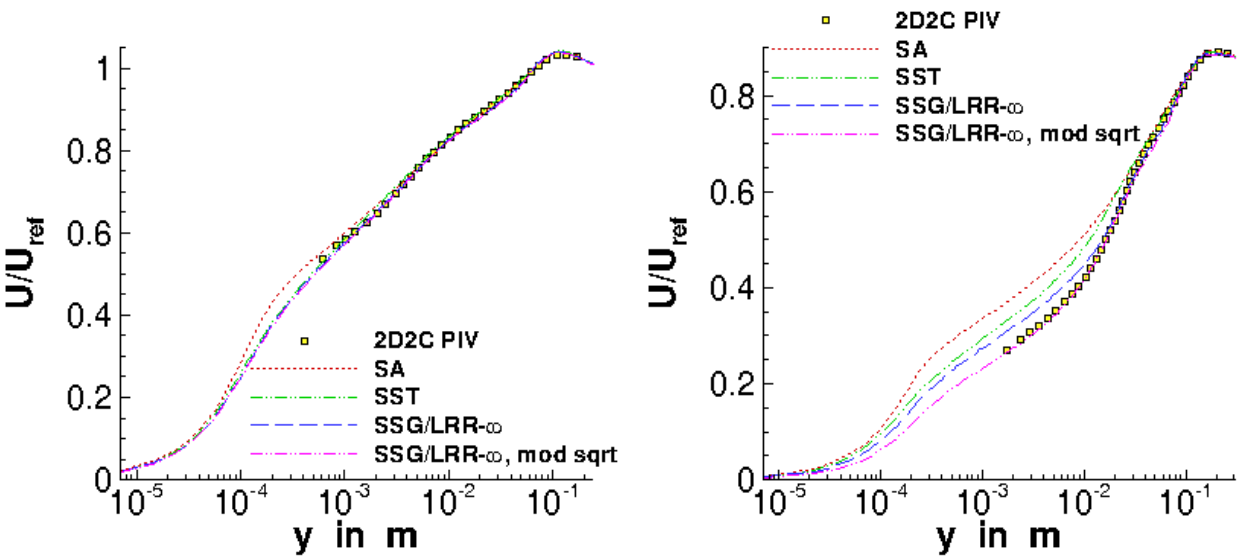

Figure 8 – Mean velocity at $x = 9.85\,\mathrm{m}$ in the region of streamwise changing pressure gradient from favourable to adverse in the region of curvature (left) and at $x = 10.41\mathrm{m}$ in the APG region (right).

SSG/LRR-ω model are close to each other and close to the experimental data. The SA model predicts a slightly higher mean velocity in the near-wall region.

For the region of the strong adverse pressure gradient, figure 8 (right) shows the mean velocity profiles at $x = 10.41\mathrm{m}$, and figure 9 (left) gives the results at $x = 10.47\,\mathrm{m}$. The discrepancies between the models and the experimental data become larger. The SSG/LRR-ω model predicts a lower mean velocity in the region $y < 0.01\mathrm{m}$ (or $y < 0.05\delta_{99}$) than the SA model and the SST model. But it can be seen that even the SSG/LRR-ω model overestimates the mean velocity in the near-wall compared to the experimental data, see figure 6 (right). The skin friction coefficient c_f in the region of the strong APG as the flow approaches separation is shown in figure 9 (right). The SSG/LRR-ω model predicts a little larger values than the experimental data, whereas the SA model and the SST model predict even larger values. For all models considered the point of flow separation point is predicted too far downstream.

We now consider the predictions of the modified SSG/LRR-ω model using the pressure diffusion term to account for the sqrt-law behaviour at APG. The modification leads to a reduction of the mean velocity in the near wall region. This leads to a good agreement with the experimental data for the position $x = 10.41\,\mathrm{m}$, see figure 8 (right), and a slightly underestimated mean velocity in the near-wall region for the position $x = 10.47\,\mathrm{m}$, see figure 9 (left). For the modified SSG/LRR-ω model, the predicted values for c_f are lower than for the original model, and are found to be a little lower than the experimental results.

The modified SSG/LRR-ω model predicts the separation point in good agreement with the experimental data. Flow separation was observed at $x = 10.83\mathrm{m}$ at midspan in the wind-tunnel experiment, which was inferred from the 2D2C PIV data for the mean velocity. However, the issue of separation deserves some words of caution. The present simulations are only 2D simulations of the flow in the centerplane of the wind-tunnel, and assume a homogeneous flow in spanwise direction. However, the experimental data indicate a spanwise variation of the separation line, which is, at least in parts, influenced by side-wall effects. In future work, simulations of the full three-dimensional wind-tunnel are planned using the SSG/LRR-ω model. In these simulations, the formation of side wall separation and the vortices in the junction of the contour model and the spanwise wind-tunnel walls should be accounted for, at least qualitatively. Moreover, this includes the displacement effect of the side wall boundary layers, which cause a flow acceleration in the centerplane at mid-span. This can be expected to increase the c_f-values in the centerplane and to cause to a downstream shift of the separation point for the three-dimensional simulations compared to the two-dimensional simulation results.

The displacement thickness δ^* predicted by the modified SSG/LRR-ω model is a little larger than for

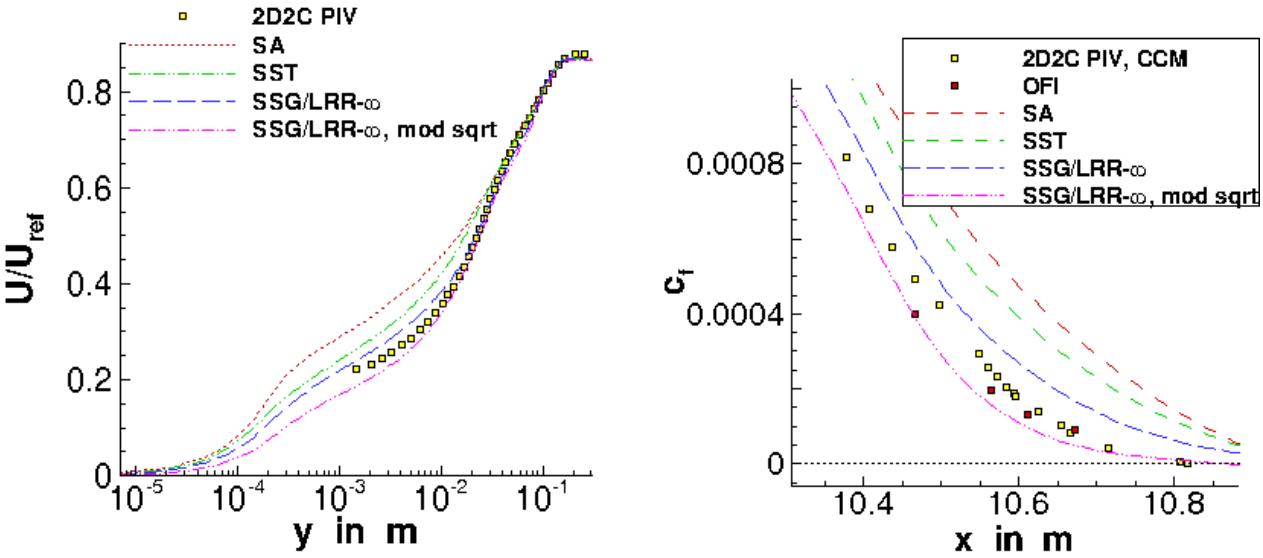

Figure 9 – Left: Mean velocity profiles at $x = 10.47\,\mathrm{m}$ in the APG region. Right: Detail view of the c_f-distribution in the region of strong adverse pressure gradient and separation.

the original model in the adverse pressure gradient region. This improves the agreement with the experimental data, see figure 6 (right). The values predicted for the shape factor $H_{12} = \delta^*/\theta$ are also slightly increased for the modified model, improving the agreement with the experimental data, see figure 7 (left).

7. Conclusions

First results of a new turbulent boundary layer experiment at a strong adverse pressure gradient and with a thin separation bubble were presented. Regarding the mean velocity profile, the log-law was confirmed to be a robust feature, even for large values of the pressure gradient parameter. A half-power law was found to emerge above the log-law. To account for these findings on the wall-law in the SSG/LRR-ω RANS turbulence model, a modification of the ω-equation for adverse-pressure gradients was proposed, based on the idea of a pressure-diffusion model, which increases the dissipation in the inner layer with increasing adverse pressure gradient. For the two-dimensional simulations of the experiment in the wind-tunnel in the mid-span centerplane, an improved agreement with the experimental data was found. However, an influence of three-dimensional flow effects due to the spanwise finite wind-tunnel geometry is expected. Therefore three-dimensional simulations including the entire test-section and all viscous wind-tunnel walls will be performed as a next step. The extensive experimental data base acquired in the framework of the described DLR VicToria project is subject of ongoing analysis, in particular, with regard to temporal behaviour of the APG TBL flow as it undergoes flow separation.

8. Acknowledgement

The authore are grateful to Prof. Manhart for providing his DNS data. The cooperation with N. Reuther, F. Eich, C. Kähler, M. Zippert, M. Tegeler, D. Schwamborn, C. Grabe and S. Görtz is gratefully acknowledged.

9. Contact Author Email Address

For future contacts, mailto: Tobias.Knopp@dlr.de

10. Copyright Statement

References

[1] A. E. Alving and H. H. Fernholz, "Mean-velocity scaling in and around a mild, turbulent separation bubble," *Phys. Fluids*, vol. 7, pp. 1956–1969, 1995.

[2] R. Johnstone, G. N. Coleman, and P. R. Spalart, "The resilience of the logarithmic law to pressure gradients: evidence from direct numerical simulation," *J. Fluid Mech.*, vol. 643, pp. 163–175, 2010.

[3] P. A. Durbin and B. A. P. Reif, *Statistical theory and modelling for turbulent flows*. Chichester: John Wiley & Sons, 2001.

[4] D. E. Coles and E. A. Hirst, *Computation of Turbulent Boundary Layers - 1968 AFOSR-IFP-Stanford Conference*. Thermosciences Division, Department of Mechanical Engineering, Stanford University, 1969.

[5] Y. Maciel, K. S. Rossignol, and J. Lemay, "A study of a separated turbulent boundary layer in stalled-airfoil-type flow conditions," *Exp. Fluids*, vol. 41, pp. 573–590, 2006.

[6] C. Atkinson, A. J. Buchner, M. Eisfelder, V. Kitsios, and J. Soria, "Time-resolved PIV measurements of a self-similar adverse pressure gradient turbulent boundary layer," in *18th International Symposium on the Application of Laser and Imaging Techniques to Fluid Mechanics, Lisbon, Portugal, July 4-7, 2016*, 2016.

[7] D. M. Schatzman and F. O. Thomas, "An experimental investigation of an unsteady adverse pressure gradient turbulent boundary layer: embedded shear layer scaling," *J. Fluid Mech.*, vol. 815, pp. 592–642, 2017.

[8] J.-H. Lee and H. J. Sung, "Effects of an adverse pressure gradient on a turbulent boundary layer," *Int. J. Heat Fluid Flow*, vol. 29, pp. 568–578, 2008.

[9] V. Kitsios, A. Sekimoto, C. Atkinson, J. A. Sillero, G. Borell, A. G. Gungor, J. Jimenez, and J. Soria, "Direct numerical simulation of a self-similar adverse pressure gradient turbulent boundary layer at the verge of separation," *J. Fluid Mech.*, vol. 829, pp. 392–419, 2017.

[10] G. N. Coleman, C. L. Rumsey, and P. R. Spalart, "Numerical study of turbulent separation bubbles with varying pressure gradient and Reynolds number," *J. Fluid Mech.*, vol. 847, pp. 28–70, 2018.

[11] V. Baskaran, A. J. Smits, and P. N. Joubert, "A turbulent flow over a curved hill. Part 1. Growth of an internal boundary layer," *J. Fluid Mech.*, vol. 182, pp. 47–83, 1987.

[12] T. Knopp, D. Schanz, A. Schröder, M. Dumitra, R. Hain, and C. J. Kähler, "Experimental investigation of the log-law for an adverse pressure gradient turbulent boundary layer flow at Re_θ up to 10000," *Flow, Turbul. Combust.*, vol. 92, pp. 451–471, 2014.

[13] T. Knopp, D. Schanz, A. Schröder, N. A. Buchmann, C. Cierpka, R. Hain, and C. J. Kähler, "Experimental investigation of a turbulent boundary layer at adverse pressure gradient at Re_θ up to 10000 using large-scale and long-range microscopic particle imaging," in *WALLTURB Workshop: Progress in Wall Turbulence: Understanding and modelling, 18.- 20. June 2014, Lille, France*, M. Stanislas, J. Jimenez, and I. Marusic, Eds. Springer Netherlands, 2014, pp. 271–281.

[14] T. Knopp, N. Reuther, M. Novara, E. Schülein, D. Schanz, A. Schröder, and C. J. Kähler, "Investigation of a turbulent boundary layer flow at high Reynolds number using particle-imaging and implications for RANS modeling," in *Tenth International Symposium on Turbulence and Shear Flow Phenomena (TSFP10) July 6-9, 2017, Swissotel, Chicago-IL, USA*, 2017.

[15] T. Knopp, N. Reuther, M. Novara, D. Schanz, E. Schülein, A. Schröder, and C. J. Kähler, "Experimental analysis of the log law at adverse pressure gradient (under review)," *J. Fluid Mech.*, vol. X, pp. xxx–xxx, 2021.

[16] T. Knopp, "A new wall-law for adverse pressure gradient flows and modification of k-ω type RANS turbulence models," 2016, aIAA Paper 2016-0588.

[17] T. Knopp, M. Novara, D. Schanz, R. Geisler, F. Philipp, A. Schröder, C. Willert, and A. Krumbein, "Modification of the ssg/lrr-omega rsm for turbulent boundary layers at adverse pressure gradient with separation using the new dlr victoria experiment," in *New Results in Numerical and Experimental Fluid Mechanics. Contributions to the 21th STAB/DGLR Symposium Darmstadt, Germany 2018*, A. Dillmann, G. Heller, E. Krämer, C. Wagner, C. Tropea, and S. Jakirlic, Eds. Springer, 2018.

[18] P. Dengel and H. H. Fernholz, "An experimental investigation of an incompressible turbulent boundary layer in the vicinity of separation," *J. Fluid Mech.*, vol. 212, pp. 615–636, 1990.

[19] M. M. M. E. Telbany and A. J. Reynolds, "Velocity distributions in plane turbulent channel flows," *J. Fluid Mech.*, vol. 100, pp. 1–29, 1980.

[20] T. B. Nickels, “Inner scaling for wall-bounded flows subject to large pressure gradients,” *J. Fluid Mech.*, vol. 521, pp. 217–239, 2004.

[21] A. E. Perry, J. B. Bell, and P. N. Joubert, “Velocity and temperature profiles in adverse pressure gradient turbulent boundary layers,” *J. Fluid Mech.*, vol. 25, pp. 299–320, 1966.

[22] B. van den Berg, “A three-dimensional law of the wall for turbulent shear flows,” *J. Fluid Mech.*, vol. 70, pp. 149–160, 1975.

[23] M. S. Rao and H. A. Hassan, “Modeling turbulence in the presence of adverse pressure gradients,” *J. Aircraft*, vol. 35, pp. 500–502, 1998.

[24] F. R. Menter, “Two-equation eddy-viscosity turbulence models for engineering applications,” *AAIA J.*, vol. 32, pp. 1598–1605, 1994.

[25] R.-D. Cecora, R. Radespiel, B. Eisfeld, and A. Probst, “Differential Reynolds-Stress Modeling for Aeronautics.” *AAIA J.*, vol. 53, pp. 739–755, 2015.

[26] B. Eisfeld, C. Rumsey, and V. Togiti, “Verification and validation of a second-moment-closure model,” *AAIA J.*, vol. 54, pp. 1524–1541, 2016.

[27] M. L. Shur, P. R. Spalart, M. K. Strelets, and A. Travin, “A hybrid RANS-LES approach with delayed-DES and wall-modelled LES capabilities,” *Int. J. Heat Fluid Flow*, vol. 29, pp. 1638–1649, 2008.

[28] D. Schanz, S. Gesemann, and A. Schröder, “Shake-The-Box: Lagrangian particle tracking at high particle image densities,” *Exp. Fluids*, vol. 70, p. 57, 2016.

[29] M. Novara, D. Schanz, N. Reuther, C. J. Kähler, and A. Schröder, “Lagrangian 3D particle tracking in high-speed flows: Shake-The-Box for multi-pulse systems,” *Exp. Fluids*, vol. 57, pp. 128 1–20, 2016.

[30] M. Novara, D. Schanz, R. Geisler, S. Gesemann, C. Voss, and A. Schröder, “Multi-exposed recordings for 3D Lagrangian particle tracking with multi-pulse Shake-The-Box,” *Exp. Fluids*, vol. 60, pp. 44–63, 2019.

[31] C. E. Willert, “High-speed particle image velocimetry for the efficient measurement of turbulence statistics,” *Exp. Fluids*, vol. 56, no. 1, 2015.

[32] A. Schröder, D. Schanz, M. Novara, F. Philipp, R. Geisler, J. Agocs, T. Knopp, M. Schroll, and C. E. Willert, “Investigation of a high Reynolds number turbulent boundary layer flow with adverse pressure gradients using PIV and 2d- and 3d- Shake-The-Box,” in *19th International Symposium on Applications of Lasers and Imaging Techniques to Fluid Mechanics*, Lisbon, Portugal, July 2018.

[33] M. Manhart and R. Friedrich, “DNS of a turbulent boundary layer with separation,” *Int. J. Heat Fluid Flow*, vol. 23, pp. 672–581, 2002.

[34] D. C. Wilcox, *Turbulence modeling for CFD*. La Canada: DWC Industries, 1998.

[35] D. Schwamborn, T. Gerhold, and R. Heinrich, “The dlr tau-code: Recent applications in research and industry,” in *European Conference on Computational Fluid Dynamics, ECCOMAS CFD 2006*, P. Wesseling, E. Onate, and J. Periaux, Eds., TU Delft, The Netherlands, 2006.

[36] R. C. Swanson and E. Turkel, “On central-difference and upwind schemes,” *Journal of Computational Physics*, vol. 101, pp. 292–306, 1992.

[37] T. Knopp and A. Probst, “An algebraic sensor for the RANS-LES switch in delayed detached-eddy simulation,” in *New Results in Numerical and Experimental Fluid Mechanics VIII*, ser. Notes on Numerical Fluid Mechanics and Multidisciplinary Design, vol. 121, 2013, pp. 457–464.

[38] A. Probst, R. Radespiel, and T. Knopp, “Detached-eddy simulation of aerodynamic flows using a Reynolds-stress background model and algebraic RANS/LES sensors,” 2011, aIAA Paper 2011-3206.

[39] S. Reuß, “A Grid-Adaptive Algebraic Hybrid RANS/LES Method,” PhD thesis, Universität Göttingen, Institut für Numerische und Angewandte Mathematik, 2015, Tech. Rep., 2015.